Evidencing fast, massive, and reversible H+ insertion in nanostructured TiO2 electrodes at neutral pH. Where do protons come from?

Kim, Yee-Seul; Kriegel, Sébastien; Harris, Kenneth D.; Costentin, Cyrille; Limoges, Benoît; Balland, Véronique

Publisher's version / Version de l'éditeur:
https://doi.org/10.1021/acs.jpcc.7b02395
The Journal of Physical Chemistry C, 121, 19, pp. 10325-10335, 2017-04-28

NRC Publications Record / Notice d'Archives des publications de CNRC:
https://nrc-publications.canada.ca/eng/view/object/?id=2356e53c-b3e7-498c-aa84-5ca19ac7491b
https://publications-cnrc.canada.ca/fra/voir/objet/?id=2356e53c-b3e7-498c-aa84-5ca19ac7491b

THE JOURNAL OF PHYSICAL CHEMISTRY C

Article

pubs.acs.org/JPCC

Evidencing Fast, Massive, and Reversible H^+ Insertion in Nanostructured TiO_2 Electrodes at Neutral pH. Where Do Protons Come From?

Yee-Seul Kim,[†] Sébastien Kriegel,[†] Kenneth D. Harris,[‡,§,∥] Cyrille Costentin,[†] Benoît Limoges,*[,†] and Véronique Balland*[,†]

[†]Laboratoire d'Electrochimie Moléculaire, UMR CNRS 7591, Université Paris Diderot, Sorbonne Paris Cité, 15 rue Jean-Antoine de Baïf, Paris F-75205 Cedex 13, France

[‡]NRC National Institute for Nanotechnology, Edmonton, Alberta T6G 2M9, Canada

[§]Department of Mechanical Engineering, University of Alberta, Edmonton, Alberta T6G 2V4, Canada

[∥]Leibniz-Institute für Polymerforshung Dresden, 01069 Dresden, Germany

Supporting Information

ABSTRACT: Ongoing developments of sustainable energy technologies based on high-surface-area semiconductive metal oxide electrodes operating under mild and safe aqueous conditions require deep understanding of proton and electron transfer/transport throughout their porous structure. To address this issue, we investigated the electrochemical reductive protonation of high surface area nanostructured amorphous TiO_2 electrodes (produced by glancing angle deposition) in both buffered and unbuffered aqueous solutions. Quantitative analysis of the two charge storage mechanisms was achieved, allowing proper deconvolution of the electrical double-layer capacitive charge storage from the reversible faradaic one resulting from the proton-coupled reduction of bulk TiO_2. We evidence that this latter process occurs reversibly and extensively (up to an intercalation ratio of 20%) not only under strongly acidic pH conditions but also, more interestingly, under neutral pH with the intercalated proton arising from the buffer rather than water. Moreover, we show that in comparison with reductive Li^+ intercalation the proton-coupled electron charge storage occurs more rapidly (in a few seconds). This important finding suggests that a high-rate and high-power charge storage device could potentially be achieved with the reversible H^+-coupled charge/discharge process in TiO_2 at neutral pH, opening thus new opportunities to the development of eco-friendly batteries for electrical energy storage.

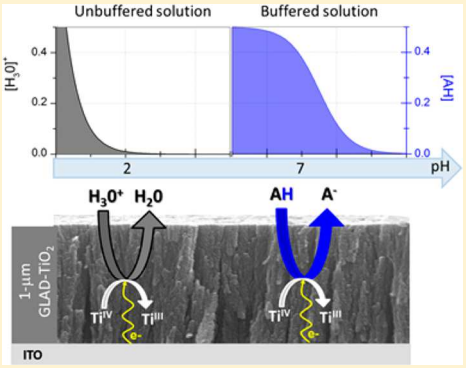

INTRODUCTION

TiO_2-based mesoporous semiconductive electrodes have attracted exponentially increasing attention in the past decades. The unique electrical, optical, and chemical properties of TiO_2 (including low-cost, high availability, low toxicity, and excellent chemical/photochemical stability) make it a prime candidate in the large-scale fabrication of transparent high-surface area electrodes and also enable an increasing range of applications in which mesoporous TiO_2 electrodes play a central role.[1,2] Among the most promising applications are the dye-sensitized solar cells (DSSC),[3] rechargeable lithium-ion batteries,[4,5] gas sensors,[6] electrochromic smart windows,[7] self-cleaning surfaces,[8] and photo(electro)catalytic processes for fuel generation[9,10] or pollutant remediation.[11] A large fraction of these applications typically require operation in dry, aprotic organic solvents (e.g., DSSC or lithium-ion batteries), which leads to issues for the environment and safety and in some cases for long-term stability. With the increasing demand for eco-friendly and sustainable technologies, there is thus a need to work toward systems operating in aqueous electrolytes and ideally under noncorrosive conditions. Consequently, growing efforts have been made recently toward the design of TiO_2-based aqueous DSSCs[12,13] and aqueous ion-insertion batteries[14,15] but also the development of TiO_2-based photoelectrocatalytic aqueous cells for water splitting,[9] CO_2 reduction,[10] biocatalysis,[16] and biosensing.[17]

Significantly, many of the above applications incorporate complex processes of charge carrier generation, separation, transport, and recombination in the metal oxide films which are currently not fully understood and predictable. This is particularly true for mesoporous TiO_2 electrodes operating in aqueous media, wherein the complex interplay between electron and proton transfer/transport strongly influences the material's behavior. It is indeed well-admitted that upon

Received: March 14, 2017
Revised: April 19, 2017
Published: April 28, 2017

DOI: 10.1021/acs.jpcc.7b02395
J. Phys. Chem. C 2017, 121, 10325−10335

applying negative bias to a TiO_2 electrode in strongly acidic conditions (pH < 2) protons have the ability to not only adsorb at the TiO_2/solution interface but also intercalate within the metal oxide lattice according to reaction 1.[1]

$$TiO_2 + xe^- + xH^+ \rightleftarrows H_xTiO_2 \quad (1)$$

(where x is the maximal mole fraction of protons that can be inserted in the metal oxide lattice)

This process is also often referred to as electrochemical doping of the semiconductor. It has been reported over a wide range of TiO_2 film morphologies and crystallinities, mostly anatase nanocrystalline films[18] or nanotube arrays,[19−21] but also rutile,[22] mixed anatase−rutile,[23,24] nanostructured films, and amorphous TiO_2 nanotube arrays.[21] Accordingly, proton insertion/intercalation appears as a general feature of mesoporous TiO_2 films.

By analogy to Li^+ intercalation in TiO_2, proton intercalation is assumed to result from local compensation of the loss of charge that is generated during the formal reduction of Ti^{IV} sites into Ti^{III} in the bulk material,[24] a process associated with a strong electrochromic effect for which interpretation is still a matter of debate.[18,22,24−26] Proton intercalation can thus be expected, similarly to Li^+, to lead to a strong increase of the electron storage capacity of TiO_2 under accumulation conditions.[27,28] In contrast to Li^+ intercalation in TiO_2 that has been the subject of intense research due to its fundamental role in lithium-ion intercalation batteries,[5] H^+ insertion in TiO_2 has been much less investigated, and many questions remain unanswered. For instance, the insertion speed, reversibility, and long-term cyclability have not been determined. It is moreover not clear which parameters influence the extent of proton insertion, at which potential it occurs, and if strongly acidic condition is a necessary prerequisite.

The purpose of the present work is to answer these questions by investigating the electrochemical reductive protonation of nanostructured films of amorphous TiO_2 in aqueous solution in the presence of either a strong acid (HCl) in an unbuffered solution or a weak acid in a neutral buffered solution (HEPES buffer). Nanostructured TiO_2 films were prepared by glancing angle deposition (GLAD) on planar ITO conductive substrates, a vacuum-based physical vapor deposition method allowing well-controlled and reproducible batch-to-batch sample fabrication.[29] GLAD-TiO_2 films also have the advantage of an open, solution-accessible porosity, allowing a relatively free and fast diffusion of chemical species throughout the void volume of the film. These nanostructured transparent TiO_2 electrodes are thus quite advantageous for quantitative analyses of factors that may affect the coupled proton−electron transfer/transport in TiO_2 using combined optical/electrochemical techniques such as cyclic voltabsorptometry.[30] As will be shown in the present work, we were able to clearly distinguish between two charge storage mechanisms. The first is purely capacitive and related to charging of the electrical double-layer capacitance when the electrode is converted to its fully conductive state at negative bias potentials. The second storage mechanism occurs at a well-defined formal potential, negative with respect to the conduction band, and corresponds to a faradaic process associated with reductive proton intercalation in the solid phase of TiO_2. We demonstrate that this faradaic electron storage process is fast, electrochemically reversible, and diffusion controlled and occurs extensively at a well-defined potential not only under unbuffered strong acidic conditions but also, more remarkably, under neutral pH conditions in a buffered solution.

MATERIALS AND METHODS

Chemicals and Materials. HEPES, HEPES sodium salt (puriss. p.a.), and lithium perchlorate (puriss. p.a.) were purchased from Sigma-Aldrich. Potassium chloride (Merck & Co., puriss. p.a.) and HCl (VWR prolabo, 37%) were used as received. All aqueous solutions were prepared with highly purified water (18.2 MΩ·cm) obtained from a TKA MicroPure UV purification system.

GLAD-TiO_2 Mesoporous Electrodes. Mesoporous 1 μm TiO_2 thin films were prepared on commercial tin-doped indium oxide (ITO) conducting glass (Delta Technologies, 8−12 Ω/□) by the glancing angle deposition (GLAD) method followed by thermal treatment. Briefly, TiO_2 films were deposited from TiO_2 evaporant (Cerac, 99.9% pure rutile) in an electron-beam physical vapor deposition system (Axxis, Kurt J Lesker). Throughout the deposition, substrates were maintained at a 72° angle with respect to impinging evaporant flux while rotating as a feedback-controlled function of the deposition rate. Following deposition, TiO_2 was annealed at 100 °C for 24 h to ensure stoichiometric TiO_2 films and, as a result, to enhance and stabilize the optical transmission of the film. Prior to electrochemical experiments, the electrodes were treated with UV/O_3 (UV/O_3 Procleaner plus, Bioforce nanosciences) for 15 min and further cleaned by subsequent immersion at room temperature in acetone and ethanol for 15 and 30 min, respectively. A portion of the TiO_2 surface was then delimited with an insulating layer to define square working electrode areas of 0.30 ± 0.02 cm^2 (evaluated from a set of N = 10 independent electrodes). In the case of experiments conducted in HEPES buffer, GLAD-TiO_2 electrodes were first washed in water and then pre-equilibrated in a 50 mM HEPES buffer solution (including 0.3 M KCl, pH 7.0) overnight before use.

Spectroelectrochemistry. The spectroelectrochemical experiments were performed in a one-compartment electrochemical cell using an Autolab PGSTAT-12 potentiostat controlled by GPES-4 software and coupled to a TORUS UV−visible spectrophotometer (Ocean Optics) equipped with optical fibers and a balanced deuterium tungsten source (Micropack). During experiments, the electrochemical cell was thermostatted at a constant temperature of 25 °C using a dedicated Peltier heater (Quantum Northwest). The potentiostat and spectrophotometer were synchronized through an input trigger signal generated by the potentiostat, thus allowing simultaneous recording of the optical absorbance and current as a function of the time-varying potential applied to the working GLAD-TiO_2 electrode. Electrodes were inserted in a 1 cm path-length quartz cell, and the working TiO_2-coated ITO electrodes were positioned perpendicular to the optical path in the cell. The cell was filled with 1.2 mL of buffer solution and thoroughly degassed by bubbling argon (for at least 20 min) prior to each experiment. A Ag/AgCl electrode in 3 M KCl (WPI, Dri-ref, + 0.2 V vs NHE at 25 °C) was used as the reference electrode, and a Pt wire was used as the counter electrode. Unless otherwise stated, all noted potentials are with respect to the Ag/AgCl reference electrode. Integration time was fixed to 3 ms, and satisfactory signal-to-noise ratios were obtained by averaging 7 scans for experiments performed at 50 $mV{\cdot}s^{-1}$ and 100 $mV{\cdot}s^{-1}$ or 4 scans for experiments performed at 200 $mV{\cdot}s^{-1}$ to 1 $V{\cdot}s^{-1}$. The average value of ohmic drop compensation was 45 ± 9 Ω (N = 12). During experiments,

DOI: 10.1021/acs.jpcc.7b02395
J. Phys. Chem. C 2017, 121, 10325−10335

argon was continuously flowed over the solution. Experimental reproducibility is attested by the good overlap of cyclic voltamograms recorded under identical experimental conditions for different GLAD-TiO_2 electrodes arising from different GLAD deposition batches (Figure S1, relative standard deviation RSD < 5%, N = 7). The reproducibility of the corresponding cyclic voltabsorptograms was not as good (RSD < 40%), suggesting a higher sensitivity of the absorbance measurement to batch-to-batch variations in the GLAD-TiO_2 samples. Experimental derivative cyclic voltabsorptograms were smoothed using a second-order Savizky−Golay algorithm.

RESULTS AND DISCUSSION

GLAD-TiO_2 Films. All experiments were carried out with 1 μm thick amorphous TiO_2 mesoporous films deposited by glancing angle deposition (deposition angle of 72°) on flat conductive ITO surfaces (Figure 1). Nanostructured GLAD-

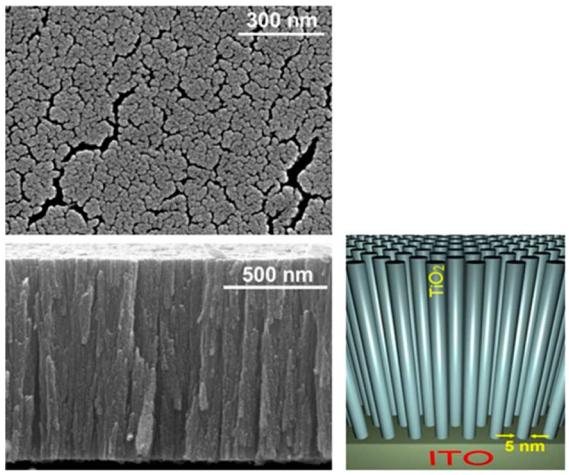

Figure 1. SEM images (top and side views) of the 1 μm GLAD-TiO_2 films. The right cartoon is a schematic representation of the film consisting of an array of homogeneously distributed cylindrical nanorods. The indicated diameter (5 nm) was calculated based on BET measurements of surface area and characterizes the high surface area fine structure internal to TiO_2 columns grown by GLAD.

TiO_2 films exhibit a high density of vertically aligned nanosized columnar structures, with a well-opened mesoporosity and controlled film thickness. From the volumetric mass density of the film (i.e., 2.5 g·cm^{-3}) and the bulk density of compact amorphous GLAD-TiO_2 film (3.8 g·cm^{-3} for a TiO_2 film prepared with a 0° deposition angle),[29] a film porosity P of 0.34 can be estimated. A film surface area enhancement (SA) of 540 per μm of film thickness was deduced from BET krypton gas adsorption isotherms.[29] It has been previously established that SA increases linearly with film thickness,[29,31] while nanorod diameter and intercolumn spacing follow power-law growth patterns.[32] In order to estimate the mean nanorod diameter (that is difficult to infer from Figure 1), we have considered a simplified geometrical representation of the GLAD films by assuming an array of uniform cylindrical nanorods homogeneously distributed perpendicular to the underlying flat ITO surface. According to this simplified picture, the mean nanorod diameter d and nanorod surface density δ were roughly estimated from both P and SA by solving the following set of two linear equations: $SA = \pi d(10^{-4} + d/4)\delta$ and $1 - P = \pi d^2\delta/4$. Using the experimentally determined values of P and SA, the mean nanorod diameter and number density of 5 nm and 3.3 × 10^{12} cm^{-2} were calculated, respectively.

Spectroelectrochemical Studies in Aqueous Solution. GLAD-TiO_2 electrodes were investigated by the coupled techniques of cyclic voltammetry and cyclic voltabsorptometry, which allow simultaneous monitoring of electrical current and optical absorbance changes for TiO_2 electrodes during cyclic potential scans at the semiconductive films.[30] Experiments were conducted in aqueous solutions containing a fixed concentration of KCl (0.3 M) as a supporting electrolyte.[33] The influence of different concentrations of two soluble proton donors was studied, either (*i*) free protons (i.e., H_3O^+) resulting from the addition of HCl in water (pH values ranging from 7 to 1.85, equivalent thus to [H_3O^+] concentrations ranging from 10^{-7} to 0.014 M) or (*ii*) the acidic AH form of the HEPES buffer at pH 7 (the concentration of which was altered by changing the buffer concentration C_B from 0 to 0.86 M with [AH] = C_B/1.3 at pH 7). The simultaneously recorded cyclic voltammograms (CVs) and cyclic voltabsorptograms (CVAs, monitored at 780 nm) under different proton donor concentrations and pHs are reported in Figures 2, S2, and

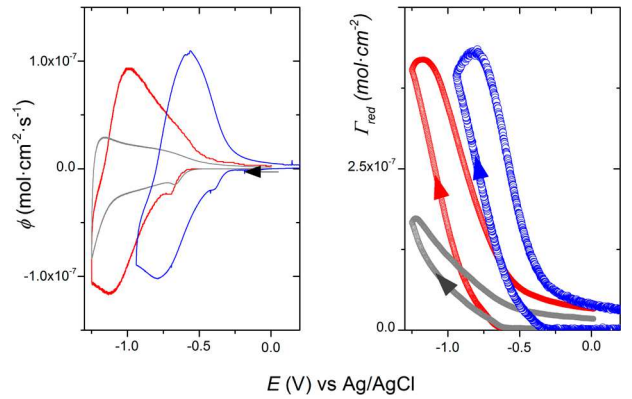

Figure 2. (Left) CVs and (right) CVAs (monitored at 780 nm) recorded simultaneously at a 1 μm thick GLAD-TiO_2 electrode in an aqueous solution of (blue) 14 mM HCl (pH 1.85) or buffered solutions (pH 7.0) of (black) 1 mM HEPES or (red) 100 mM HEPES. All solutions also contained 0.3 M KCl as supporting electrolyte. Electrodes were scanned from 0 to −1.25 V at pH 7 and from 0 to −0.96 V at pH 1.85. CVs are expressed in flux density and CVAs in surface concentrations (i.e., $\Delta A_{780}/(1000\cdot\varepsilon_{780})$). Scan rate: 0.1 V·s^{-1}. T = 25 °C.

S3. Cyclic scans were systematically initiated at anodic potentials where the semiconductive TiO_2 films were insulating. The potential was then increased to sufficiently cathodic potentials where TiO_2 was fully converted into a metal-like conductive film, and then the potential sweep was reversed to recover the initial insulating state. During the charging process (forward scan), all CVs and CVAs share some common features (Figures 2, S2, and S3). First of all, the current recorded at the beginning of the forward cathodic scan is very small and nearly constant, engendering no significant absorbance change at 780 nm. These observations indicate that TiO_2 behaves as an insulator within this potential window and that the small recorded current on the CVs only arises from the double-layer charging capacitance of the underlying exposed ITO surface. At negative potentials to −0.60 V at pH 7.0 (or −0.30 V at pH 1.85), the exponential increase of current in CVs reflects both the progressive filling of electronic

DOI: 10.1021/acs.jpcc.7b02395
J. Phys. Chem. C 2017, 121, 10325−10335

states that are localized in traps distributed in the band gap of TiO_2 and the filling of extended conduction band states when the applied potential becomes sufficiently negative (i.e., when it is raised close to the TiO_2 conduction band edge potential of $E_{CB} \sim -0.75$ V vs Ag/AgCl at pH 7.0 or −0.45 V vs Ag/AgCl at pH 1.85).[25] This transition thus characterizes the increase of the Fermi level of electrons in the TiO_2 film and also the transition from an insulating to a conductive state by increasing the chemical capacitance (C_{chem}) of the semiconductive material. (To preserve the electrical neutrality, negative charges accumulated in TiO_2 are assumed to be compensated by electrosorption of cations at the metal−oxide interface).[1,34] This process is associated with a simultaneous increase of the TiO_2 film absorbance monitored at 780 nm. Accumulated electrons can thus be quantitatively analyzed in CVs through the exponential increase of current occurring from an onset potential less negative than E_{CB} but also in CVAs through absorbance increase in the near-IR region from the same onset potential (an increase which linearly scales with the amount of electrons accumulated in the semiconductive material).[18,26] As attested by complete restoration of the initial metal oxide transparency upon scanning the potential back in the anodic direction, the charging/discharging process is fully reversible under the present experimental conditions, indicating complete removal of all injected charges. The onset potential at which both current and absorbance start to increase is pH dependent, showing a 60 mV anodic shift per unit of pH decrease, fully consistent with the reported Nernstian pH dependence of the TiO_2 conduction band edge.[35,36] The potential at which the amorphous GLAD-TiO_2 electrode becomes fully degenerate at pH 7.0 (i.e., at $E < -0.75$ V vs Ag/AgCl, corresponding also to the transition from the exponential growth of the current to a constant double-layer capacitive current) is also consistent with the E_{CB} reported for sintered nanoparticulate films of anatase at the same pH (−0.8 V vs SCE).[25] One may however notice that the onset potential at which the film transitions from an insulating to a conductive state is steadily downshifted as the scan rate is increased, suggesting a transition process which does not occur at thermodynamic equilibrium within the range of scan rates explored (0.05 to 0.5 $V \cdot s^{-1}$). It seems thus that there is a kinetic barrier in the delivery of electrons to the semiconductive material that for the moment we cannot clearly interpret and which is beyond the scope of this work.

Once the applied potential lies within the potential window corresponding to the fully conductive state of TiO_2, shapes and magnitudes of both CVs and CVAs exhibit strong differences and changes as a function of the proton donor concentration (Figures 2, S2, and S3). Two distinct behaviors can be clearly identified as detailed below.

Low Proton Donor Concentrations (Unbuffered Aqueous Solutions of pH > 3.5 or Poorly Buffered Aqueous Solutions with [AH] < 5 mM). For very low acid concentrations and for potentials more negative than the conduction band edge of TiO_2, CVs display a rectangular-shaped current response almost independent of the applied potential and scaling linearly with the scan rate v (Figures 2 and also Figures S2 and S3 wherein CVs are normalized to the scan rate). This behavior is typical of the double-layer capacitive charging current that can be recorded at a high surface area electrode immersed in an inert supporting electrolyte (differing from the chemical capacitive charging current by its independence from the applied potential). This is corroborated in CVAs by the near overlap of absorbance change between the forward and backward potential scans at 0.1 $V \cdot s^{-1}$ (absence of significant hysteresis), a behavior that is reminiscent of a fast charging/discharging of a double-layer capacitive current. Since the double-layer capacitance (C_{dl}) is connected in series with the chemical capacitance, it can only be assessed when $C_{chem} \gg C_{dl}$ (i.e., at potentials more negative than the E_{CB} of TiO_2).[30,34]

It is worth mentioning that CVs normalized to v at neutral pH (Figure S2) do not all completely overlap in the lowest range of negative potentials; under −1.1 V, a small rise of current is observed and accompanied by a concomitant increase in absorbance at 780 nm. We assume that this arises not from the hydrogen evolution reaction (HER) as often assumed but from the reductive coloration of the underlying ITO substrate, a phenomenon that was recently ascribed to the reductive formation of metallic nanoparticles of indium and tin at the ITO surface and which strongly depends on the electrolyte composition and pH.[37,38] Control CV experiments were thus performed at bare ITO electrodes under the same experimental conditions as those for GLAD-TiO_2 electrodes, and the same increases in current and absorbance were observed at potentials more negative than −1.0 V (not shown).

The above results allowed us to conclude that when the applied potential is more negative than E_{CB} and when there is no significant concentration of free protons or weak acid in solution the GLAD-TiO_2 electrode behaves like a high surface area electrical capacitor. Assuming that at low proton donor concentration the CV current is purely capacitive at pH 7.0 in the potential window −0.7 to −1.1 V, an average electrical capacitance density of 18 ± 2 $mF \cdot cm^{-2}$ (i.e., normalized to the geometric electrode area) can be inferred (which also corresponds to a specific double-layer capacitance of 72 $F \cdot g^{-1}$), which is far more than expected for a standard flat conductive electrode in an electrolyte solution (10−40 $\mu F \cdot cm^{-2}$).[39,40] The value is, however, consistent with the large specific surface area generated by the quasi-metallic GLAD-TiO_2 films at these potentials. Once corrected for film surface area enhancement (i.e., 540 μm^{-1}), an intrinsic capacitance density of 33 $\mu F \cdot cm^{-2}$ was found for the degenerate semiconductive film, a value that is close to the theoretical one (10−20 $\mu F \cdot cm^{-2}$) calculated for a flat conductive surface in an aqueous electrolyte solution.[41] The measured capacitance density, however, is in the lower end of values previously reported for nanocrystalline films of TiO_2 in aprotic solvents (30−120 $\mu F \cdot cm^{-2}$),[42−44] which is unsurprising in light of the fact that all of the previously reported intrinsic capacitances were determined in the presence of lithium cations. These cations complicate the accurate estimation of the true capacitive contribution on account of their intercalating faradaic contribution to the current. Another factor that can also significantly affect a reliable evaluation of the intrinsic capacitance density is the extent of correlation between the inner surface area of the nanostructured electrode (i.e., measured using the BET measurement, see Materials and Methods section) and the effective electroactive surface area.

High Proton Donor Concentrations (Unbuffered Aqueous Solutions with pH < 3.5 or Buffered Aqueous Solutions with [AH] > 5 mM). Upon either increasing the buffer concentration (up to 860 mM at pH 7) or decreasing the pH below pH 3, the shapes and magnitudes of current/absorbance changes in CVs/CVAs are strongly modified and increased for cathodic potentials wherein TiO_2 is conductive (Figures 2, S2, and S3). The strong increase in current is linked to the growth of a broad reversible wave on top of the

DOI: 10.1021/acs.jpcc.7b02395
J. Phys. Chem. C 2017, 121, 10325−10335

capacitive current. Depending on the pH, this reversible wave is centered on formal potentials ($E^{0\prime}$) of −1.06 V vs Ag/AgCl at pH 7.0 (0.1 M HEPES) and −0.68 V vs Ag/AgCl at pH 1.85 (Figure 2 and Table S1), exhibiting thus a shift of −74 mV per unit of pH, which is again reminiscent of the −60 mV pH dependence of the E_{CB} of TiO_2.[1,36] The current of this reversible wave is clearly not proportional to the scan rate as shown from CVs normalized to v in Figures S2 and S3. In order to further analyze this wave, CVs recorded at different proton donor concentrations were systematically corrected for the electrochemical double-layer capacitance contribution by subtracting the CVs obtained under negligible proton donor concentration (i.e., by subtracting the CVs in 0.3 M KCl). Once corrected for capacitive current and normalized to $v^{1/2}$, the resulting CVs gathered in Figure S4 show good overlap, especially in terms of magnitudes of cathodic and anodic peaks. These results clearly demonstrate that the reversible wave is proportional to $v^{1/2}$ over the entire range of buffer concentrations and pHs investigated in this work (Figure 3),

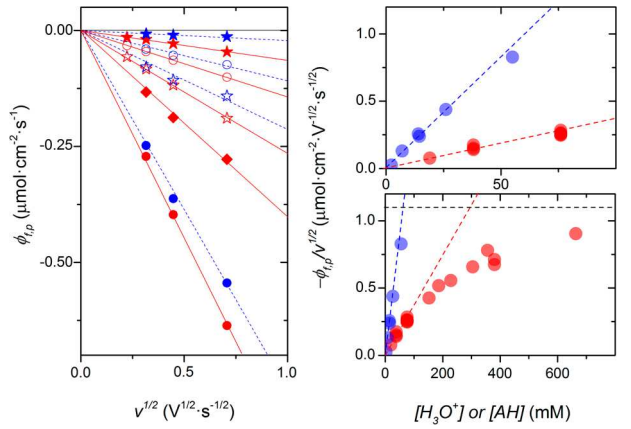

Figure 3. (Left) Cathodic peak electron flux density in CV as a function of $v^{1/2}$ (for scan rates ranging from 0.05 to 0.5 V·s^{-1}) and for different concentrations of (blue data) free protons, i.e., [H_3O^+] = (solid blue star) 2.5, (blue open circle) 7, (open blue star) 14, and 50 (solid blue circle) mM or (red data) the acidic form of HEPES buffer, i.e., [AH] = (solid red star) 19, (red open circle) 38, (red open star) 77, (red solid diamond) 153, and (red solid circle) 656 mM. (Right) Cathodic peak electron flux density normalized to $v^{1/2}$ and plotted as a function of proton donor concentration: (blue) free protons and (red) the acidic form of HEPES buffer. Dashed lines correspond to the linear regression fits of eq 5 to the data determined at low proton donor concentrations. The horizontal dotted black line corresponds to the extrapolated limiting value of $\phi_{f,p}/v^{1/2}$.

a behavior that strongly supports the occurrence of a reversible faradaic process rate-limited by a diffusion-controlled mass transport. On account of its $E^{0\prime}$ position, strong dependence on proton donor concentration, and also diffusion-controlled response, the reversible wave can be reasonably ascribed to the reversible faradaic reduction of Ti^{IV} sites in the metal oxide lattice coupled with proton uptake for local charge compensation. Depending on the experimental conditions, this proton-coupled electron transfer reaction, when fast, can be assumed to be rate-limited either by the solid-state diffusion of protons inserted within the TiO_2 lattice or by the solution diffusion of proton donors in the bulk electrolyte. This process is formally equivalent to the Li^+-coupled electron transfer reaction occurring in intercalation metal oxide materials, a process that has been and continues to be widely studied based on its great importance in the field of Li-ion batteries.[4,5] Compared to the CVs reported in the literature for Li^+ intercalation in nanocrystalline TiO_2 films, it is remarkable here to note the rather high electrochemical reversibility of proton intercalation (characterized by a small potential separation between the anodic and cathodic peaks, i.e., ΔE_p < 0.23 at 0.1 V·s^{-1}, see Table S1), as compared to corresponding reports for Li^+-intercalation in nanocrystalline TiO_2 films (ΔE_p > 0.4 V at CV scan rates <10 mV·s^{-1}).[43−45] The poor reversibility of lithium-ion intercalation is often associated with crystallographic phase changes during the faradaic process, so the good electrochemical reversibility we observed here for H^+ intercalation suggests that crystallographic variations may not be a major issue. The disordered structure and defects in amorphous TiO_2 may also contribute to facilitate the interfacial proton-coupled electron transfer reaction.

In order to get deeper insights into the diffusion-limited faradaic charge storage process, the electron flux density of the cathodic peak $\phi_{f,p}$, normalized to $v^{1/2}$, was plotted as a function of the proton donor concentration (Figure 3). Provided that the proton donor concentration in solution remains low, the data clearly show a linear relationship which is indicative of a process rate-controlled by the diffusional mass transport of proton donors in the electrolyte. Upon further increasing the proton donor concentration (i.e., >100 mM), a progressive deviation from linearity with a tendency to asymptotically reach a maximal value at high buffer concentrations is well-discerned at pH 7.0. That the diffusion-controlled cathodic peak current is independent of the proton donor concentration at high buffer concentrations, but still proportional to $v^{1/2}$, allows us to conclude that the faradaic process is now rate-controlled by the solid-state diffusion of protons within the TiO_2 lattice, rather than by the mass transport of proton donor in solution (the latter being sufficiently fast to support the redox process at the interface under these conditions). Such a transition from one limiting case to the other was unfortunately not observable under acidic pH conditions for the reason that we were unable to perform CV experiments at pH < 1.0 without generating an irreversible loss of the electrical properties of TiO_2 together with a concomitant and permanent coloration of the metal oxide film. (This blue/black coloration was observed after exceeding a certain charge accumulation threshold or upon scanning the potential into excessively negative values.) Such an abrupt alteration of the physicochemical properties of TiO_2 might be related to a significant structural/morphological change of the metal oxide lattice, which under strong electron/proton accumulation may lead to delamination or breakage/collapse of the GLAD-TiO_2 film.

From the above experimental observations, it can be concluded that the charging/discharging process related to the reversible proton-coupled reduction of Ti^{IV} ions can, depending on the experimental conditions, be rate-limited by any of (i) the mass transport of proton donor in solution, (ii) the solid-state diffusion of protons in the TiO_2 lattice, (iii) the interfacial proton-coupled electron transfer, or (iv) a mixed control of these different processes (Scheme 1).

Another important finding from the above results is that the aqueous solvent is an ineffective proton donor in comparison to the acidic form of HEPES or H_3O^+. This might be explained by the very low acidity of water (pK_a = 14 which is 6.5 orders of magnitude higher than the pKa of the HEPES buffer), which would suggest that the thermodynamic ease with which the

DOI: 10.1021/acs.jpcc.7b02395
J. Phys. Chem. C 2017, 121, 10325−10335

Scheme 1. Schematic Representation of the Faradaic Charging Processes Occurring at the TiO_2 Mesoporous Electrodes Involving Proton−Coupled Electron Transfer to Solvent-Accessible Ti^{IV} Ions According to the Interfacial Reactions 2 or 3, Depending on the Proton Provider, Followed by Coupled Electron/Proton Diffusion Within the TiO_2 Lattice According to Reaction 4

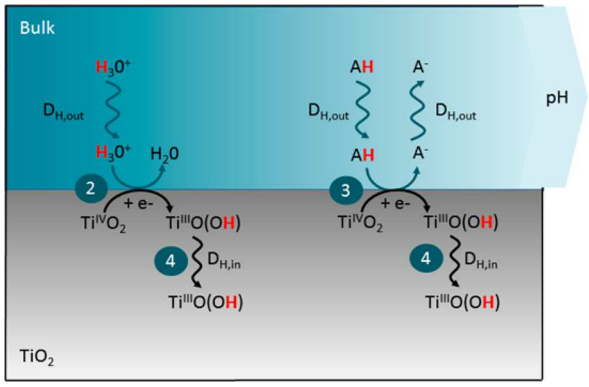

proton donor can deliver a proton to the metal oxide is a key factor in the proton intercalation mechanism.

Intercalation Process. The proton-coupled reduction of Ti^{IV} is assumed to be induced at the metal oxide/electrolyte interface. It thus involves the soluble proton donor locally available at this interface, which according to the experimental conditions can be either free protons in solution or the acidic form [AH] of the buffer (in the present case, the zwitterionic protonated form of HEPES). We can thus write the following electron transfer reactions at the metal oxide interface for each proton donor

$$Ti^{IV}O_2 + e^- + H_3O^+ \rightleftarrows Ti^{III}(O)(OH) + H_2O \quad (2)$$

$$Ti^{IV}O_2 + e^- + AH \rightleftarrows Ti^{III}(O)(OH) + A^- \quad (3)$$

These reactions are expected to occur more favorably at grain boundaries where interfacial Ti^{IV} sites are more accessible and solvent exposed.[46] According to the high specific surface area of GLAD-TiO_2 electrodes and the high surface concentration of Ti^{IV} ions, these reactions are assumed to provoke massive consumption of the proton donor present at the metal oxide/electrolyte interface (i.e., in the void volume of the porous film). Under these circumstances, consumption is sufficient to rapidly induce rate limitation by the mass transport of proton donor from the bulk solution. This is especially true when the working concentration of the proton donor is low, thus leading to a current response of the diffusion-controlled reversible wave linearly dependent on the soluble proton donor concentration.

Once surface Ti^{IV} sites are reduced and charge compensated by protonation, we can assume that the paired electron/proton couple (e^-/H^+) can be transferred between adjacent titanium ions localized in the subsurface region of the amorphous TiO_2 material, formally according to the following electron−proton transfer reaction

$$Ti^{IV}O_2 + Ti^{III}(O)(OH) \rightleftarrows Ti^{III}(O)(OH) + Ti^{IV}O_2 \quad (4)$$

This mechanism of charge transfer propagation throughout the metal oxide lattice can be assumed to be equivalent to a diffusion-like process considering an isotropic random walk of e^-/H^+ throughout the TiO_2 lattice. (It is worth noting that in this process electrons may not originate from hopping electron transfer reactions between adjacent titanium ions but rather from transfer with electrons accumulated in the delocalized states of the conduction band. Therefore, during this e^-/H^+ migration, only protons can truly be considered to hop between adjacent titanium sites.) To determine the rate of this solid-state diffusion-like process, it is essential to ensure that the mass transport of proton donor in solution does not play a role. Such a situation is encountered in Figure 3 when the magnitude of the reversible wave is nearly independent of the proton donor concentration.

The linear relationship observed between $\phi_{f,p}/v^{1/2}$ and the soluble proton donor concentration, [H], at low and intermediate concentrations in Figure 3 (i.e., <100 mM) is typically associated with the first situation where the diffusion-controlled reversible current response is limited by mass transport of the proton donor. If we assume a Nernstian interfacial reaction (i.e., a fast reversible proton-coupled electron transfer reaction), the following Randles−Sevcik equation can applied for both reactions 2 and 3 at low proton donor concentrations[40,47]

$$\frac{\phi_{f,p}}{v^{1/2}} = \frac{i_{f,p}}{FSv^{1/2}} = 0.4463\sqrt{\frac{F}{RT}}\sqrt{D_{H,out}}[H] \quad (5)$$

where $\phi_{f,p}$ and $i_{f,p}$ are the faradaic peak flux density ($C \cdot mol^{-1} \cdot cm^{-2}$) and peak current (A), respectively; v is the scan rate ($V \cdot s^{-1}$); S is the delimited geometric electrode area (or projected electrode area, cm^2); $D_{H,out}$ is the diffusion coefficient of proton donor in the bulk aqueous solution ($cm^2 \cdot s^{-1}$); and [H] is the concentration of proton donor in solution ($mol \cdot cm^{-3}$). The geometric electrode area is utilized in this equation due to the fact that the diffusion layer thickness of the soluble proton donor is much larger than the 1 μm film thickness of GLAD-TiO_2 within the range of scan rates used in the present study. From the linear regression fit of eq 5 to the linear part of experimental plots in Figure 3, it becomes possible to determine the diffusion coefficient $D_{H,out}$ of each proton donor we have investigated. Diffusion coefficients of 3×10^{-5} $cm^2 \cdot s^{-1}$ and 1.5×10^{-6} $cm^2 \cdot s^{-1}$ were found for H_3O^+ and the protonated form of HEPES, respectively. These values are in good agreement with the diffusion coefficient values reported in the literature (i.e., 2.3×10^{-5} $cm^2 \cdot s^{-1}$ for H_3O^+[48,49] and 6.2×10^{-6} $cm^2 \cdot s^{-1}$ for HEPES,[50] both at 25 °C).

In highly concentrated solutions of proton donor it was not possible to definitely reach the limiting case where $\phi_{f,p}$ is uniquely rate-controlled by the apparent diffusion of H^+ in TiO_2; however, the apparent diffusion coefficient of protons within the metal oxide lattice could be estimated from the maximal electron flux density that was extrapolated at high buffer concentrations in Figure 3 (dotted black line). Under this limiting case, eq 5 no longer applies and must be modified to consider reaction 4 as the rate-limiting diffusion-like process. On account of the small solid-state diffusion coefficients reported for cations in TiO_2 (10^{-13}−10^{-17} $cm^2 \cdot s^{-1}$),[42−44,51−55] the diffusion length of H^+ within the bulk metal oxide is expected to be much smaller than the smallest dimension of nanorods (5 nm diameter) such that the proton gradient can be considered as a semi-infinite linear diffusion-like process occurring normal to the metal oxide interface (i.e., normal to the vertical walls of the nanorods). Under these conditions, the

DOI: 10.1021/acs.jpcc.7b02395
J. Phys. Chem. C 2017, 121, 10325−10335

following Randles–Sevcik equation can be used (assuming again a Nernstian redox reaction)

$$\frac{\phi_{f,p}}{v^{1/2}} = \frac{i_{f,p}}{FSv^{1/2}} = 0.4463\sqrt{\frac{F}{RT}}\frac{S_e}{S}\sqrt{D_{H,in}}xC_{Ti}^{0} \quad (6)$$

where S_e (in cm^2) is here the specific electroactive surface area of the mesoporous electrode; $D_{H,in}$ (in $cm^2 \cdot s^{-1}$) is the apparent diffusion coefficient of H^+ within the metal oxide lattice; C_{Ti}^{0} (0.048 $mol \cdot cm^{-3}$) is the maximal concentration of titanium ions in amorphous TiO_2; and x is the maximal mole fraction of protons that can be inserted in the fully reduced phase H_xTiO_2. This equation can thus be used to calculate the diffusion coefficient of H^+ within the TiO_2 lattice using the limiting value of $\phi_{f,p}/v^{1/2}$ extrapolated in Figure 3 (dotted black line, $\phi_{f,p}/v^{1/2} = 1.1 \times 10^{-6}$ mol $cm^{-2} \cdot s^{-1/2} \cdot V^{-1/2}$). Two issues must, however, be considered. First, an appropriate estimate of the maximal value of x must be available. Unfortunately, we were experimentally unable to reach full reduction of TiO_2 before permanent failure of the GLAD-TiO_2 electrode. The second issue is related to the difficulty of reliably evaluating the true specific electroactive surface area, S_e, through which the proton-coupled charge transfer occurs, an area which does not necessarily correspond to that determined by BET. This is indeed supported by the idea that ion insertion may not occur homogeneously at the electrolyte/metal oxide interface but preferentially via percolation channels within single grains, as has been recently demonstrated by nanoscale imaging of a lithium titanate surface at various states of Li^+ intercalation.[56] Consequently, the diffusion coefficient for ion intercalation determined from eq 6 is an apparent value (one can finally hardly deconvolute the two parameters contained in the $S_e \times D_{H,in}^{1/2}$ product).

Assuming $S_e/S = SA = 540$ (estimated from BET) for the 1 μm thick GLAD-TiO_2 film and a mole fraction $x = 0.5$ by analogy to that usually reported for Li^+ in anatase,[5,52] an apparent solid-state proton diffusion coefficient of $D_{H,in} = 10^{-15}$ $cm^2 \cdot s^{-1}$ is obtained. From such a value, the penetration length, l, of protons within the metal oxide lattice during the time course of a typical CV experiment can be estimated using eq 7, where t is the charging time of the experiment.

$$l = \sqrt{\pi D_{H,in} t} \quad (7)$$

At the slowest scan rate (0.1 $V \cdot s^{-1}$) we have used, and for the highest buffer concentration (860 mM HEPES at pH 7), a proton penetration length l of 1.25 nm was calculated. This diffusion length is less than the smallest dimension of GLAD-TiO_2 nanorods (~5 nm) we have roughly estimated from our simple model in Figure 1, a result which therefore justifies *a posteriori* the validity of eq 6 and, therefore, the assumption of 1D semi-infinite linear diffusion. It also suggests that for the strongest accumulation conditions we were able to reach, the concentration gradient layer of reduced Ti^{IV} extends from the TiO_2 nanorod walls up to ~40% of the total metal oxide volume.

Comparative Study with Lithium Intercalation. With the aim of directly comparing proton-ion versus lithium-ion insertion in a 1 μm thick amorphous GLAD-TiO_2 film, a series of CV and CVA experiments were performed in aqueous electrolytes containing either 76 mM Li^+ (pH ~ 6.5) or 76 mM acid form of HEPES (pH 7.0) for a set of scan rates (Figure S5). The marked differences between the shapes of CVs (and also CVAs) recorded in the presence of a proton ion donor and those recorded in the presence of lithium ion suggest that Li^+ intercalation does not proceed as fast as proton intercalation under the selected conditions. One may argue that at the low Li^+ concentration used the lack of discernible lithium intercalation within GLAD-TiO_2 films would result from a slow diffusion rate of Li^+ in the bulk of solution, leading thus to a low faradaic current response according to eq 5. This is however unlikely because the diffusion coefficient of Li^+ in aqueous solution is quite high (~10^{-5} $cm^2 \cdot s^{-1}$),[57] and so its diffusion rate in water is even faster than the AH form of HEPES. Still, an additional CV experiment was performed at a much higher concentration of Li^+ (1 M) (Figure S5), but again the small increase of current compared with that obtained with a proton donor such as the protonated form of HEPES at 0.66 M definitely indicates the much slower insertion of Li^+ than H^+ in the amorphous film of GLAD-TiO_2. One should note that the broad and small reversible waves we observed here for Li^+ intercalation in amorphous GLAD-TiO_2 are in line with previous reports of Li^+ intercalation in other types of amorphous mesoporous TiO_2 films in aprotic solvents, exhibiting a similar broad and small reversible wave in CV, much smaller and less well-defined than for Li^+ intercalation in mesoscopic films of pure anatase.[51,58] All of these observations allow us to conclude that, under our conditions, proton ion insertion occurs in amorphous mesoporous GLAD-TiO_2 films through a remarkably faster and more favorable process than lithium-ion insertion.

On account of the above observations, it is interesting to return to the value we have determined for the solid-state diffusion coefficient of protons in GLAD-TiO_2 ($D_{H,in} = 10^{-15}$ $cm^2 \cdot s^{-1}$) because it is the key parameter governing the proton charge storage dynamics in TiO_2 relative to lithium. Analyzing in detail the solid-state diffusion coefficients of Li^+ reported in the literature (in particular those obtained at nanoporous TiO_2 films made of 7–8 nm anatase particles) allows us to identify consistent values in the range of 1×10^{-17} to 6×10^{-17} $cm^2 \cdot s^{-1}$.[42,43,51] Assuming these data as the most relevant for direct comparison to the present value of $D_{H,in}$ in GLAD-TiO_2, we can conclude that protons diffuse 20- to 100-fold faster in amorphous TiO_2 than Li^+ in anatase. This strong difference may explain the obvious contrast we observe between proton and lithium-ion insertion in amorphous GLAD-TiO_2 electrodes.

Charge Storage. One great advantage of cyclic voltabsorptometry lies in the correlation that can be done between electrochemical and spectroscopic data. In the present study, it allows for real-time analysis of the spectroscopic features of TiO_2 films during the electrochemical charging process. Assuming that all injected electrons give rise to absorbance at 780 nm, cyclic voltabsorptograms can be converted to derivative cyclic voltabsorptograms (DCVA) according to eq 8 (where both current and absorbance are expressed in flux density ϕ in $mol \cdot cm^{-2} \cdot s^{-1}$) and directly compared to each other.

$$\phi = \frac{1}{1000\varepsilon_{780}}\frac{dA_{780}}{dt} = \frac{i}{FS} \quad (8)$$

where A_{780} is the absorbance monitored at 780 nm and ε_{780} in $M^{-1} \cdot cm^{-1}$ is the extinction coefficient of the stored electron.

As shown in Figure S6, when using an extinction coefficient value of 800 or 1200 $M^{-1} \cdot cm^{-1}$ at 780 nm, depending on the electrode batch, a perfect overlap of the DCVAs and CVs is

DOI: 10.1021/acs.jpcc.7b02395
J. Phys. Chem. C 2017, 121, 10325–10335

obtained over the entire potential window, regardless of the pHs and buffer concentrations. The independence of ε_{780} from both the applied potential as well as the proton provider is *a priori* surprising since it indicates that all electrons stored within the material share common spectroscopic features in the visible range, regardless of their origin or nature (i.e., either the electrons are associated with the filling of electronic states in the band gap and/or conduction band, or stored in the double-layer capacitance at the TiO_2−electrolyte interface, or associated with the faradaic charging process leading to the reductive protonation of Ti^{IV} ions within the TiO_2 lattice). Such an observation seems to contradict a previous report in the literature suggesting that electrons associated with lithium-ion insertion in TiO_2 have a marked increase in average extinction coefficient (in the near-IR range) with respect to electrons accumulated in the conduction band.[35] This previous report, however, was performed under strong accumulation conditions, which are known to lead to a long lasting coloration of the metal oxide film. In the present study, such strong accumulation conditions are not encountered. The extinction coefficient values used in the present study, 900 ± 300 $M^{-1}\cdot cm^{-1}$, are in good agreement with those previously found under different experimental conditions and for different types of mesoporous TiO_2 films.[18,25,35]

The charge density Q (in $C\cdot cm^{-2}$) stored in the 1 μm thick GLAD-TiO_2 film can be easily determined for each electrode either from the maximum absorbance change monitored at 780 nm or from integration of the charging/discharging current in CV, using eq 9.

$$Q = F\frac{\Delta A_{780}}{1000\varepsilon_{780}} = F\int\frac{i}{S}\mathrm{d}t \tag{9}$$

This equation was used to estimate the total charge stored at the highest tested concentration of proton donor (0.66 M AH in 0.86 M HEPES buffer, pH 7) and 0.1 $V\cdot s^{-1}$ (Figure 4). A value of 78 $mC\cdot cm^{-2}$ was obtained, corresponding thus to a total charge capacity of 310 $C\cdot g^{-1}$. This total stored charge results from the combined contributions of charges stored from faradaic reduction of TiO_2 and charges accumulated at the double-layer interface of the nanostructured metal oxide. The charge fraction associated with the faradaic contribution can be determined by subtraction of charge accumulated in the absence of significant proton intercalation (corresponding to the double-layer capacitance charge) from the total charge. From the magnitude of absorbance changes recorded at the lowest concentration of proton donor, a capacitive charge density of 18 $mC\cdot cm^{-2}$ (or 72 $C\cdot g^{-1}$) could be recovered. This implies that 23% of the total stored charge results from the double-layer capacitance of the nanoporous TiO_2 film, while the remaining 77% (i.e., 60 $mC\cdot cm^{-2}$ or 240 $C\cdot g^{-1}$ or 66 $mA\cdot h\cdot g^{-1}$) arises from the proton-coupled electron transfer reaction within the metal-oxide network (Table 1). This latter value is equivalent to 0.6 $\mu mol\cdot cm^{-2}$ of intercalated protons and thus corresponds to the reductive protonation of ∼20% of the total titanium ions in the lattice (equivalent to a x value of 0.2). As the charging process is diffusion-limited under the experimental conditions, the maximal mole fraction x is manifestly not reached. It could theoretically be attained experimentally by either decreasing the scan rate or prolonging the time the electrode is biased at negative potentials ($<E^{0\prime}$). However, the scan rate could not be decreased below 0.05 $V\cdot s^{-1}$ in the present study without the strong charge accumulation condition inducing a sudden irreversible failure of the GLAD-TiO_2 electrodes (see above).

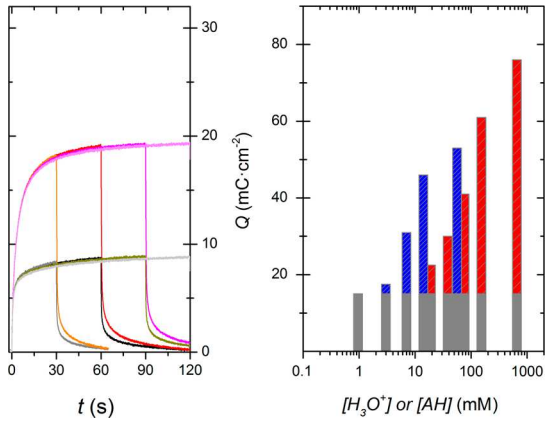

Figure 4. (Left) Double potential step chronoabsorptometric responses (the absorbance has been converted into charge per unit of geometric electrode area using eq 9) monitored at 780 nm in a 0.3 M KCl aqueous solution containing (black and gray lines) 1 mM or (orange, red, magenta, pink lines) 100 mM HEPES at pH 7. The potential was stepped from 0.0 to −1.0 V and then back to 0.0 V (vs Ag/AgCl). The double potential step experiment was repeated several times by progressively increasing both the cathodic and anodic polarization time from 30 to 120 s. (Right) Charge contributions of the (gray) double-layer charging and (blue and red) faradaic proton intercalation to the total charge stored in a GLAD-TiO_2 film during a CV performed at 0.1 $V\cdot s^{-1}$. Bars in blue are for free protons, while those in red are for the acidic form, AH, of the HEPES buffer.

Despite the inability to reach the maximum mole fraction, it is still possible to compare the total e^-/H^+ charges that could be reversibly stored in the 1 μm thick GLAD-TiO_2 electrode against previous reports for Li^+ storage in various mesoporous anatase films (in aprotic solvents) (Table 1). It is remarkable to note in Table 1 that under our experimental conditions proton ion insertion within amorphous GLAD-TiO_2 films occurs nearly as extensively as lithium-ion intercalation in mesoporous crystalline films of anatase. Moreover, this extensive proton insertion is achieved much more rapidly than reported for lithium-ion insertion (the 0.2 mole fraction was attained here at a scan rate of 100 $mV\cdot s^{-1}$, while for Li^+, the 0.15 to 0.31 mole fractions were obtained at 0.5 $mV\cdot s^{-1}$; see Table 1). Interestingly, in spite of completely different experimental conditions, a similarly extensive reductive protonation of TiO_2 (∼16%) was obtained by prolonged UV-irradiation in toluene of amorphous nanoparticles capped with organic ligands.[59]

To better characterize the long-term stability, reversibility, and speed of e^-/H^+ charge/discharge in GLAD-TiO_2, mesoporous films were investigated by double potential step chronoabsorptometric experiments in HEPES buffer at two different proton donor concentrations (i.e., 0.77 and 77 mM AH). To avoid excessive charge accumulation, the forward potential was stepped from 0.0 to −1.0 V, a moderate cathodic potential only slightly more positive than the formal potential ($E^{0\prime}$ = −1.06 V) of the reversible proton insertion/disinsertion wave. In the absence of significant proton donor in solution, the time-course absorbance change in Figure 4 grows rapidly until it reaches a steady state value of 8.7 $mC\cdot cm^2$ (in less than 30 s). This fast absorbance increase is representative of the electrode capacitive charging rate (i.e., the charging of both the chemical and double-layer capacitances) when there is no significant contribution of proton insertion to charge storage. At an

DOI: 10.1021/acs.jpcc.7b02395
J. Phys. Chem. C 2017, 121, 10325−10335

Table 1. Structural Characteristics and Charge Storage Properties of the Present GLAD TiO_2 Films Compared to Those Previously Established for Other Mesoporous TiO_2 Films

	GLAD film	nanoparticle films			sol−gel film
TiO_2 crystallinity	amorphous	anatase	anatase	anatase	anatase
BET surface area ($m^2 \cdot g^{-1}$)	220	220	150	350−400	180−200
nanoparticle diameter (nm)	~5[a]	7	10	4−5	nd
intercalating ion	H^+	Li^+	Li^+	Li^+	Li^+
scan rate ($mV \cdot s^{-1}$)	100	0.5	0.5	0.5	0.5
total charge stored ($C \cdot g^{-1}$)	310	490	460	200	340
electrical capacitive contribution (%)	23	55	35	50	40
ion intercalation capacity ($mA \cdot h \cdot g^{-1}$)	66	61	83	28	57
mole fraction of inserted cation	0.2	0.15	nd[b]	0.18	0.31
ref	present work	44	44	45	45

[a]Estimated from geometrical considerations (see text). [b]Not determined.

appreciable proton donor concentration of 77 mM (0.1 M HEPES), a significantly higher limiting charge storage value of 19.3 $mC \cdot cm^2$ (an increase of 120%) is reached after only slightly longer accumulation time (ca. 60 s). This result confirms the remarkably fast reductive protonation of GLAD-TiO_2 and allows for easy estimation of the additional stored charges resulting from the faradaic proton insertion at the selected applied potential. The stationary charge accumulated after 1 min of electrode polarization at −1.0 V also points to thermodynamic control of the accumulated charge (i.e., in equilibrium with the Fermi level of −1.0 V applied to the metal oxide film), which is here assumed governed by the Nernst's law. (This is a reasonable assumption when one considers the good electrochemical reversibility of the proton insertion/disinsertion waves on the CVs.) From the maximal faradaic charge density extracted in Figure 4 (i.e., $Q = 11\ mC \cdot cm^{-2}$ after subtraction of the capacitive charge density), it can be calculated that 4% of the total Ti ions present in the metal oxide film are electrochemically reduced after only 1 min of electrode polarization at −1.0 V. Inserting this ratio into the Nernst equation and assuming the law remains valid regardless of the amount of charge injected into TiO_2 allows us to estimate an x value of 0.45 (using $E^{0\prime} = -1.06$ V and $E = -1.0$ V). This maximum insertion ratio is close to the mole fraction of 0.5 found for lithiated anatase ($Li_{0.5}TiO_2$) wherein lithium ions are randomly distributed over half of the available interstitial octahedral sites.[60] It also validates *a posteriori* the x value of 0.5 used in eq 6 for the calculation of $D_{H,in}$. Another important merit of the chronoabsorptometric experiments in Figure 4 is to clearly highlight the high-rate electrochemical charging and discharging processes as well as their high reversibility and cyclability as attested by the perfect overlay of the multiple double potential-step experiments repetitively recorded.

CONCLUSION

In the present work, we demonstrate that the charge storage capacity of amorphous GLAD-TiO_2 electrodes can be strongly enhanced upon reductive protonation of lattice Ti^{IV} ions. This process is characterized by a reversible and fast faradaic proton-coupled electron transfer reaction centered at a well-defined formal potential (i.e., a well-defined localized state), energetically positioned at a value negative to the conduction band potential of TiO_2 (i.e., at a potential where TiO_2 is fully degenerate), and that we can reasonably attribute to the $Ti^{IV}O_2/Ti^{III}O(OH)$ redox couple. This reversible process can however only be revealed by the presence of a sufficiently large concentration of an appropriate proton donor in solution, i.e., free protons or a much weaker acid such as the acidic form of the buffer. We demonstrate moreover that reductive doping of amorphous mesoporous TiO_2 in aqueous solution is highly specific for protons and that Li^+ insertion does not compete with proton insertion under the present experimental conditions, most likely because of the short time window used. Despite this, the total charge stored in the GLAD-TiO_2 electrode upon proton insertion falls within the range of values reported for mesoporous TiO_2 electrodes upon lithium insertion in aprotic solvent.

The present study is of special interest for the development of devices operating under mildly aqueous conditions as it demonstrates that electron/proton accumulation within mesoporous TiO_2 films can occur massively and rapidly at neutral pH conditions. This, in turn, indicates that high rate and high power could be achieved for reversible proton charge/discharge storage within the material. It provides moreover an easy methodology to distinguish the faradaic current density related to proton intercalation from that associated with the classical electrical capacitance by modifying the concentration of the weak acid.

ASSOCIATED CONTENT

Supporting Information

The Supporting Information is available free of charge on the ACS Publications website at DOI: 10.1021/acs.jpcc.7b02395.

Figures S1 to S6 (CVs and CVAs recorded at different scan rates in the presence of increasing concentrations of strong or weak acid and lithium, DCVAs) and Table S1 (PDF)

AUTHOR INFORMATION

Corresponding Authors

*E-mail: veronique.balland@univ-paris-diderot.fr.
*E-mail: limoges@univ-paris-diderot.fr.

ORCID

Véronique Balland: 0000-0001-9534-9659

Author Contributions

The manuscript was written through contributions of all authors. All authors have given approval to the final version of the manuscript.

Notes

The authors declare no competing financial interest.

DOI: 10.1021/acs.jpcc.7b02395
J. Phys. Chem. C 2017, 121, 10325−10335

■ ACKNOWLEDGMENTS

Financial support for S.K. was obtained from Agence Nationale pour la Recherche (3D-BIOELEC/ANR-11-JS08-011). K.D.H. thanks Jae-Young Cho for the SEM imaging and Jeremy Sit for ongoing access to the GLAD evaporator.

■ REFERENCES

(1) Berger, T.; Monllor-Satoca, D.; Jankulovska, M.; Lana-Villarreal, T.; Gomez, R. The electrochemistry of nanostructured titanium dioxide electrodes. *ChemPhysChem* **2012**, *13*, 2824−2875.
(2) Li, W.; Wu, Z.; Wang, J.; Elzatahry, A. A.; Zhao, D. A Perspective on Mesoporous TiO_2 Materials. *Chem. Mater.* **2014**, *26*, 287−298.
(3) Hagfeldt, A.; Boschloo, G.; Sun, L.; Kloo, L.; Pettersson, H. Dye-sensitized Solar Cells. *Chem. Rev.* **2010**, *110*, 6595−6663.
(4) Reddy, M. V.; Subba Rao, G. V.; Chowdari, B. V. Metal oxides and oxysalts as anode materials for Li ion batteries. *Chem. Rev.* **2013**, *113*, 5364−5457.
(5) Dylla, A. G.; Henkelman, G.; Stevenson, K. J. Lithium Insertion in Nanostructured TiO_2 (B) Architectures. *Acc. Chem. Res.* **2013**, *46*, 1104−1112.
(6) Bai, J.; Zhou, B. Titanium dioxide nanomaterials for sensor applications. *Chem. Rev.* **2014**, *114*, 10131−10176.
(7) Nang Dinh, N.; Minh Quyen, N.; Chung, D. N.; Zikova, M.; Truong, V. Van Highly-efficient electrochromic performance of nanostructured TiO_2 films made by doctor blade technique. *Sol. Energy Mater. Sol. Cells* **2011**, *95*, 618−623.
(8) Watanabe, T.; Nakajima, A.; Wang, R.; Minabe, M.; Koizumi, S.; Fujishima, A.; Hashimoto, K. Photocatalytic activity and photoinduced hydrophilicity of titanium dioxide coated glass. *Thin Solid Films* **1999**, *351*, 260−263.
(9) Ashford, D. L.; Gish, M. K.; Vannucci, A. K.; Brennaman, M. K.; Templeton, J. L.; Papanikolas, J. M.; Meyer, T. J. Molecular Chromophore-Catalyst Assemblies for Solar Fuel Applications. *Chem. Rev.* **2015**, *115*, 13006−13049.
(10) Ma, Y.; Wang, X. L.; Jia, Y. S.; Chen, X. B.; Han, H. X.; Li, C. Titanium Dioxide-Based Nanomaterials for Photocatalytic Fuel Generations. *Chem. Rev.* **2014**, *114*, 9987−10043.
(11) Zhang, Y.; Xiong, X.; Han, Y.; Zhang, X.; Shen, F.; Deng, S.; Xiao, H.; Yang, X.; Yang, G.; Peng, H. Photoelectrocatalytic degradation of recalcitrant organic pollutants using TiO_2 film electrodes: An overview. *Chemosphere* **2012**, *88*, 145−154.
(12) Bella, F.; Gerbaldi, C.; Barolo, C.; Grätzel, M. Aqueous dye-sensitized solar cells. *Chem. Soc. Rev.* **2015**, *44*, 3431−3473.
(13) Bella, F.; Galliano, S.; Falco, M.; Viscardi, G.; Barolo, C.; Grätzel, M.; Gerbaldi, C. Unveiling iodine-based electrolytes chemistry in aqueous dye-sensitized solar cells. *Chem. Sci.* **2016**, *7*, 4880−4890.
(14) Liu, S.; Pan, G. L.; Yan, N. F.; Gao, X. P. Aqueous TiO_2/$Ni(OH)_2$ rechargeable battery with a high voltage based on proton and lithium insertion/extraction reactions. *Energy Environ. Sci.* **2010**, *3*, 1732.
(15) Liu, J.; Wang, J.; Ku, Z.; Wang, H.; Chen, S.; Zhang, L.; Lin, J.; Shen, Z. X. Aqueous Rechargeable Alkaline Co_x Ni_2 S_{2-x}/TiO_2 Battery. *ACS Nano* **2016**, *10*, 1007−1016.
(16) Hambourger, M.; Gust, D.; Hambourger, M.; Kodis, G.; Moore, A.; Moore, G. F. Solar energy conversion in a photoelectrochemical biofuel cell. *Dalton Trans.* **2009**, 9979−9989.
(17) Zhao, W.-W.; Xu, J.-J.; Chen, H.-Y. Photoelectrochemical bioanalysis: the state of the art. *Chem. Soc. Rev.* **2015**, *44*, 729−741.
(18) Berger, T.; Anta, J. A.; Morales-Florez, V. Electrons in the band gap: Spectroscopic characterization of anatase TiO_2 nanocrystal electrodes under fermi level control. *J. Phys. Chem. C* **2012**, *116*, 11444−11455.
(19) Fabregat-Santiago, F.; Barea, E. M.; Bisquert, J.; Mor, G. K.; Shankar, K.; Grimes, C. A. High carrier density and capacitance in TiO_2 nanotube arrays induced by electrochemical doping. *J. Am. Chem. Soc.* **2008**, *130*, 11312−11316.
(20) Meekins, B. H.; Kamat, P. V. Got TiO_2 Nanotubes? Lithium Ion Intercalation can Boost Their Photoelectrochemical Performance Supporting Information. *ACS Nano* **2009**, *3*, 3437−3446.
(21) Ghicov, A.; Tsuchiya, H.; Hahn, R.; MacAk, J. M.; Munoz, A. G.; Schmuki, P. TiO_2 nanotubes: H^+insertion and strong electrochromic effects. *Electrochem. Commun.* **2006**, *8*, 528−532.
(22) Berger, T.; Anta, J. A.; Morales-Flórez, V. Spectroscopic properties of electrochemically populated electronic states in nanostructured TiO_2 films: anatase versus rutile. *Phys. Chem. Chem. Phys.* **2013**, *15*, 13790−5.
(23) Idigoras, J.; Berger, T.; Anta, J. A. Modification of mesoporous TiO_2 films by electrochemical doping: Impact on photoelectrocatalytic and photovoltaic performance. *J. Phys. Chem. C* **2013**, *117*, 1561−1570.
(24) Cao, F.; Oskam, G.; Searson, P. C.; Stipkala, J. M.; Heimer, T. A.; Farzad, F.; Meyer, G. J. Electrical and optical properties of porous nanocrystalline TiO_2 films. *J. Phys. Chem.* **1995**, *99*, 11974−11980.
(25) Rothenberger, G.; Fitzmaurice, D.; Graetzel, M. Spectroscopy of conduction band electrons in transparent metal oxide semiconductor films: optical determination of the flatband potential of colloidal titanium dioxide films. *J. Phys. Chem.* **1992**, *96*, 5983−5986.
(26) Mandal, D.; Hamann, T. W. Band energies of nanoparticle semiconductor electrodes determined by spectroelectrochemical measurements of free electrons. *Phys. Chem. Chem. Phys.* **2015**, *17*, 11156−11160.
(27) Simon, P.; Gogotsi, Y.; Dunn, B. Where Do Batteries End and Supercapacitors Begin? *Science* **2014**, *343*, 1210−1211.
(28) Augustyn, V.; Simon, P.; Dunn, B. Pseudocapacitive oxide materials for high-rate electrochemical energy storage. *Energy Environ. Sci.* **2014**, *7*, 1597.
(29) Krause, K. M.; Taschuk, M. T.; Harris, K. D.; Rider, D. A.; Wakefield, N. G.; Sit, J. C.; Buriak, J. M.; Thommes, M.; Brett, M. J. Surface area characterization of obliquely deposited metal oxide nanostructured thin films. *Langmuir* **2010**, *26*, 4368−76.
(30) Renault, C.; Nicole, L.; Sanchez, C.; Costentin, C.; Balland, V.; Limoges, B. Unraveling the charge transfer/electron transport in mesoporous semiconductive TiO_2 films by voltabsorptometry. *Phys. Chem. Chem. Phys.* **2015**, *17*, 10592−10607.
(31) Renault, C.; Andrieux, C. P.; Tucker, R. T.; Brett, M. J.; Balland, V.; Limoges, B. Unraveling the mechanism of catalytic reduction of O_2 by microperoxidase-11 adsorbed within a transparent 3D-nanoporous ITO film. *J. Am. Chem. Soc.* **2012**, *134*, 6834−45.
(32) Krause, K. M.; Vick, D. W.; Malac, M.; Brett, M. J. Taking a Little off the Top: Nanorod Array Morphology and Growth Studied by Focused Ion Beam Tomography. *Langmuir* **2010**, *26*, 17558−17567.
(33) One should note that the K^+ cation present in the supporting electrolyte has not been considered as a potentially intercalating ion because of its too large size and the absence of effect on the CVs upon changing the KCl concentration.
(34) Fabregat-Santiago, F.; Mora-Seró, I.; Garcia-Belmonte, G.; Bisquert, J. Cyclic Voltammetry Studies of Nanoporous Semiconductors. Capacitive and Reactive Properties of Nanocrystalline TiO_2 Electrodes in Aqueous Electrolyte. *J. Phys. Chem. B* **2003**, *107*, 758−768.
(35) Boschloo, G.; Fitzmaurice, D. Electron Accumulation in Nanostructured TiO_2 (Anatase) Electrodes. *J. Phys. Chem. B* **1999**, *103*, 7860−7868.
(36) Lyon, L. A.; Hupp, J. T. Energetics of the Nanocrystalline Titanium Dioxide/Aqueous Solution Interface: Approximate Conduction Band Edge Variations between $H_0 = -10$ and $H_- = +26$. *J. Phys. Chem. B* **1999**, *103*, 4623−4628.
(37) Zukalova, M.; Bousa, M.; Bastl, Z.; Jirka, I.; Kavan, L. Electrochemical Doping of Compact TiO2 Thin Layers. *J. Phys. Chem. C* **2014**, *118*, 25970−25977.
(38) Liu, L.; Yellinek, S.; Valdinger, I.; Donval, A.; Mandler, D. Important Implications of the Electrochemical Reduction of ITO. *Electrochim. Acta* **2015**, *176*, 1374−1381.

DOI: 10.1021/acs.jpcc.7b02395
J. Phys. Chem. C 2017, 121, 10325−10335

(39) Zhang, Y.; Feng, H.; Wu, X.; Wang, L.; Zhang, A.; Xia, T.; Dong, H.; Li, X.; Zhang, L. Progress of electrochemical capacitor electrode materials: A review. *Int. J. Hydrogen Energy* **2009**, *34*, 4889−4899.
(40) Bard, A. J.; Faulkner, L. R. *Electrochemical Methods: Fundamentals and Applications*; Wiley, 2000.
(41) Kötz, R.; Carlen, M. Principles and applications of electrochemical capacitors. *Electrochim. Acta* **2000**, *45*, 2483−2498.
(42) Lindström, H.; Södergren, S.; Solbrand, A.; Rensmo, H.; Hjelm, J.; Hagfeldt, A.; Lindquist, S.-E. Li^+ Ion Insertion in TiO_2 (Anatase). 1. Chronoamperometry on CVD Films and Nanoporous Films. *J. Phys. Chem. B* **1997**, *101*, 7710−7716.
(43) Lindström, H.; Södergren, S.; Solbrand, A.; Rensmo, H.; Hjelm, J.; Hagfeldt, A.; Lindquist, S.-E. Li^+ Ion Insertion in TiO_2 (Anatase). 2. Voltammetry on Nanoporous Films. *J. Phys. Chem. B* **1997**, *101*, 7717−7722.
(44) Wang, J.; Polleux, J.; Lim, J.; Dunn, B. Pseudocapacitive Contributions to Electrochemical Energy Storage in TiO_2 (Anatase) Nanoparticles. *J. Phys. Chem. C* **2007**, *111*, 14925−14931.
(45) Brezesinski, T.; Wang, J.; Polleux, J.; Dunn, B.; Tolbert, S. H. Templated Nanocrystal-Based Porous TiO_2 Films for Next-Generation Electrochemical Capacitors. *J. Am. Chem. Soc.* **2009**, *131*, 1802−1809.
(46) Rahman, M. M.; Wang, J. Z.; Hassan, M. F.; Wexler, D.; Liu, H. K. Amorphous carbon coated high grain boundary density dual phase $Li_4Ti_5O_{12}$-TiO_2: A nanocomposite anode material for li-ion batteries. *Adv. Energy Mater.* **2011**, *1*, 212−220.
(47) Note: it is also possible to consider the case of a slow or irreversible electrochemical reaction by analyzing the peak current using the following expression $i_{f,p}/FS\nu^{1/2} = 0.4958\sqrt{F/RT}\sqrt{\alpha D_{H,out}}[H]$, where α is the transfer coefficient. If we assume $\alpha = 0.5$, it would mean that the constant 0.4463 in eq 1 is replaced by 0.3506 for an irreversible electrochemical reaction.
(48) Wang, J. H.; Robinson, C. V.; Edelman, I. S. Self-diffusion and Structure of Liquid Water. III. Measurement of the Self-diffusion of Liquid Water with H^2, H^3 and O^{18} as Tracers. *J. Am. Chem. Soc.* **1953**, *75*, 466−470.
(49) Lee, S. H.; Rasaiah, J. C. Proton transfer and the mobilities of the H^+ and OH^- ions from studies of a dissociating model for water. *J. Chem. Phys.* **2011**, *135*, 124505.
(50) http://www.bio.umass.edu/biology/kunkel/probe/buffers/ (accessed December 2016).
(51) Kavan, L.; Rathouský, J.; Grätzel, M.; Shklover, V.; Zukal, A. Surfactant-Templated TiO_2 (Anatase): Characteristic Features of Lithium Insertion Electrochemistry in Organized Nanostructures. *J. Phys. Chem. B* **2000**, *104*, 12012−12020.
(52) Van De Krol, R.; Goossens, A.; Schoonman, J. Spatial Extent of Lithium Intercalation in Anatase TiO_2. *J. Phys. Chem. B* **1999**, *103*, 7151−7159.
(53) Kanamura, K.; Yuasa, K.; Takehara, Z. Diffusion of lithium in the TiO_2 cathode of a lithium battery. *J. Power Sources* **1987**, *20*, 127−134.
(54) Wu, M.-S.; Wang, M.-J.; Jow, J.-J.; Yang, W.-D.; Hsieh, C.-Y.; Tsai, H.-M. Electrochemical fabrication of anatase TiO_2 nanostructure as an anode material for aqueous lithium-ion batteries. *J. Power Sources* **2008**, *185*, 1420−1424.
(55) Van der Ven, A.; Bhattacharya, J.; Belak, A. A. Understanding Li Diffusion in Li-Intercalation Compounds. *Acc. Chem. Res.* **2013**, *46*, 1216−1225.
(56) Verde, M. G.; Baggetto, L.; Balke, N.; Veith, G. M.; Seo, J. K.; Wang, Z.; Meng, Y. S. Elucidating the Phase Transformation of $Li_4Ti_5O_{12}$ Lithiation at the Nanoscale. *ACS Nano* **2016**, *10*, 4312−4321.
(57) Braun, B. M.; Weingaertner, H. Accurate self-diffusion coefficients of lithium+, sodium+, and cesium+ ions in aqueous alkali metal halide solutions from NMR spin-echo experiments. *J. Phys. Chem.* **1988**, *92*, 1342−1346.
(58) Huang, S.; Zhang, L.; Lu, X.; Liu, L.; Liu, L.; Sun, X.; Yin, Y.; Oswald, S.; Zou, Z.; Ding, F.; Schmidt, O. G. Tunable Pseudocapacitance in 3D $TiO_{2-\delta}$ Nanomembranes Enabling Superior Lithium Storage Performance. *ACS Nano* **2017**, *11*, 821−830.
(59) Schrauben, J. N.; Hayoun, R.; Valdez, C. N.; Braten, M.; Fridley, L.; Mayer, J. M. Titanium and Zinc Oxide Nanoparticles Are Proton-Coupled Electron Transfer Agents. *Science* **2012**, *336*, 1298−1301.
(60) Cava, R. J.; Murphy, D. W.; Zahurak, S.; Santoro, A.; Roth, R. S. The crystal structures of the lithium-inserted metal oxides $Li_{0.5}TiO_2$ anatase, $LiTi_2O_4$ spinel, and $Li_2Ti_2O_4$. *J. Solid State Chem.* **1984**, *53*, 64−75.

DOI: 10.1021/acs.jpcc.7b02395
J. Phys. Chem. C 2017, 121, 10325−10335